Stratocumulus Cloud-Top Height Estimates and Their Climatic Implications

PAQUITA ZUIDEMA AND DAVID PAINEMAL

Rosenstiel School of Marine and Atmospheric Sciences, University of Miami, Miami, Florida

SIMON DE SZOEKE

CIRES/University of Colorado, Boulder, Colorado

CHRIS FAIRALL

NOAA/Earth Systems Research Laboratory, Boulder, Colorado

(Manuscript received 7 July 2008, in final form 27 March 2009)

ABSTRACT

A depth-dependent boundary layer lapse rate was empirically deduced from 156 radiosondes released during six month-long research cruises to the southeast Pacific sampling a variety of stratocumulus conditions. The lapse-rate dependence on boundary layer height is weak, decreasing from a best fit of 7.6 to 7.2 K km^{-1} as the boundary layer deepens from 800 m to 2 km. Ship-based cloud-base heights up to 800 m correspond well to lifting condensation levels, indicating well-mixed conditions, with cloud bases >800 m often 200–600 m higher than the lifting condensation levels. The lapse rates were combined with Moderate Resolution Imaging Spectrometer 11-μm-derived cloud-top temperatures and satellite microwave-derived sea surface temperatures to estimate stratocumulus cloud-top heights. The October-mean cloud-top height structure of the southeast Pacific was then spatially and diurnally characterized. Coastal shoaling is apparent, but so is a significant along-coast cloud-top height gradient, with a pronounced elevation of the cloud-top heights above the Arica Bight at ~20°S. Diurnal cloud-top height variations (inferred from irregular 4-times-daily sampling) can locally reach 250 m in amplitude, and they can help to visualize offshore propagation of free-tropospheric vertical motions. A shallow boundary layer associated with the Chilean coastal jet expands to its north and west in the afternoon. Cloud-top heights above the Arica Bight region are depressed in the afternoon, which may mean that increased subsidence from sensible heating of the Andes dominates an afternoon increase in convergence/upward motion at the exit of the Chilean coastal jet. In the southeast Atlantic during October, the stratocumulus cloud-top heights are typically lower than those in the southeast Pacific. A coastal jet region can also be identified through its low cloud-top heights. Coastal shoaling of the South Atlantic stratocumulus region is mostly uniform with latitude, in keeping with the more linear Namibian/Angolan coastline. The southeast Atlantic shallow cloudy boundary layer extends farther offshore than in the southeast Pacific, particularly at 15°S.

1. Introduction

The boundary layer height of the planet's stratocumulus cloud decks is sensitive to a balance of processes that also define its cloud fraction and radiative influence. The complexity of the balance between the free-tropospheric vertical velocity, which typically but not always suppresses the boundary layer, and entrainment, which deepens but dries the boundary layer, is evident from the range of scales that must be considered. At the largest scale is free-troposphere subsidence associated with the climatological surface anticyclones. Orography and coastline features modulate the subsidence. In the southeast Pacific (SEP), the primary focus of this study, modeling studies suggest that the Andean topography increases the fetch of the large-scale subsidence into the western equatorial Pacific (e.g., Richter and Mechoso 2006; Takahashi and Battisti 2007; Xu et al. 2004). Closer to the continent, the subsidence varies at the mesoscale as well as diurnally because of sensible heating of the high, arid Andes, and the vertical velocity can even be directed upward during a time of day (Garreaud

Corresponding author address: Paquita Zuidema, RSMAS/MPO, 4600 Rickenbacker Cswy., Miami, FL 33149.
E-mail: pzuidema@rsmas.miami.edu

DOI: 10.1175/2009JCLI2708.1

and Muñoz 2004; Rutllant et al. 2003). Observations reveal that the fluctuations in vertical motion have consequences for the cloud liquid water path (O'Dell et al. 2008) and the mean cloud-deck radiative influence (Rozendaal et al. 1995). While not yet fully documented for cloud-top height, regional field experiments also suggest that stratocumulus cloud tops in the SEP vary more diurnally than those of the northeast Pacific (Bretherton et al. 2004; Garreaud et al. 2001; Minnis et al. 1992; Stevens et al. 2007).

Cloud-top entrainment processes, driven by infrared radiational cooling of the cloud-deck top, surface moisture and heat fluxes, and shear, are hypothesized to explain the transition into the trade wind cumulus regions of the lower cloud fraction (Wyant et al. 1997). The deepening of the boundary layer also encourages decoupling within the boundary layer, separating a well-mixed cloud layer from a (well mixed) subcloud layer (Betts et al. 1992; Wood and Bretherton 2004). Decoupling is commonly observed within SEP boundary layer soundings (de Szoeke et al. 2009; Kollias et al. 2004; Serpetzoglou et al. 2008).

The planetary boundary layer height also affects stratocumulus precipitation in ways that are not well characterized to date. Drizzle is common in stratocumulus regions, and particularly so in the southeast Pacific (Leon et al. 2008). The cooling and moistening of the boundary layer from evaporating drizzle below cloud base can either stabilize or destabilize the boundary layer depending upon the vertical distribution of the latent heating and thereby feedback upon the dissipation or maintenance of the cloud deck. These processes can be modulated by aerosol, which in turn impacts cloud fraction and height. Because zonal offshore continental flow can help establish the coastal boundary layer height (e.g., Muñoz 2008; Muñoz and Garreaud 2005), in places where it does so, continental aerosol must be advected along with it. Aerosol concentrations are elevated within certain regions of the SEP stratocumulus deck; however, the aerosol origin, incorporation into and impact on the stratocumulus is still under question. Cloud-top height serves as one critical test of marine boundary layer cloud simulations containing moist and/or aerosol processes (e.g., Hannay et al. 2009; Wang et al. 2004; Wyant et al. 2007).

The issues raised here point to the usefulness of a well-characterized cloud-capped boundary layer height. They also helped motivate the Variability of the American Monsoon (VAMOS) Ocean–Cloud–Atmosphere–Land Study (VOCALS), which has both a modeling focus and a regional experiment held in October–November 2008 in the southeast Pacific. The larger-scale spatial and diurnal structure of the southeast Pacific stratocumulus cloud-top heights has not yet been observationally assessed in detail. Satellite data, in theory, provide an efficient observational approach. For complex regional climates, such as the southeast Pacific, the ideal satellite technique samples a large spatial region frequently and is able to accurately resolve small vertical cloud-top height variations and its spatial gradients. Techniques such as radio occultation (e.g., von Engeln et al. 2005) can potentially provide good vertical resolution and accuracy, but at large horizontal spacings (~500-km daily). A space-based lidar, such as the Cloud–Aerosol Lidar with Orthogonal Polarization (CALIOP), despite its excellent vertical resolution and accuracy of ±30 m, samples regional domains poorly because it is swath limited. This is also a limitation of the space-based CloudSat radar (see, e.g., Zuidema and Mapes 2008).

One more conventional technique maps satellite infrared-derived cloud-top temperatures to cloud-top height. The technique is well suited to stratocumulus clouds because of their strong capping temperature inversion. While geostationary satellite data provide better diurnal sampling, the Moderate Resolution Imaging Spectroradiometer (MODIS) 11-μm-derived cloud-top temperatures benefit from the instrument's superior radiometric calibration [contrast the discussion in Várnai and Marshak (2002) to that in Brest et al. (1997) and Wang et al. (1999)]. The high radiometric accuracy allows for the resolution of small variations in cloud-top temperature, and by extension in height. Good accuracy also improves cloud detection, a prerequisite for cloud property retrievals, over that of the International Satellite Cloud Climatology Project (ISCCP). This may be particularly valuable for identifying low-lying, optically thin coastal clouds. The instrument's wide (~2300 km) swath encourages a robust view of regional features, and the 4-times-daily sampling of MODIS, although irregular, still allows for a glimpse of the diurnal cycle. Last, a MODIS cloud-top height product can be usefully combined with other MODIS cloud property retrievals for further insight into aerosol–cloud interactions.

Despite the high intrinsic value of MODIS data, its current operational cloud-top height retrieval algorithms are not well suited for stratocumulus clouds (Garay et al. 2008; Harshvardhan et al. 2009; Holz et al. 2008). We circumvent the issues with the operational retrievals by relying on radiosondes to empirically determine the relationship between cloud-top temperature and cloud-top height. Six month-long research cruises between 2001 and 2007 to the SEP (tracks shown in Fig. 1) included launches of primarily Vaisala RS-90 series radiosondes. The radiosondes allow for an empirical deduction of a depth-dependent boundary layer lapse rate. In total, the cruises launched 156 radiosondes within 1 h of the 4-times-daily MODIS overpasses under

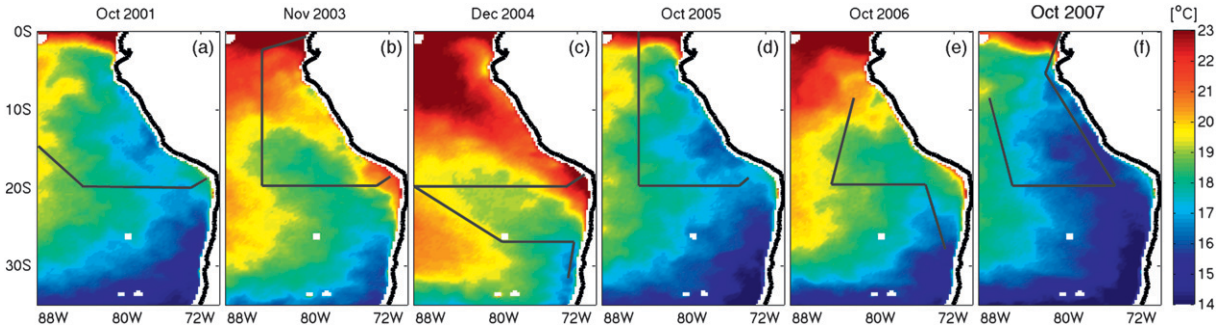

FIG. 1. Monthly mean TMI sea surface temperature with black lines indicating the ship track for the cruise during (a) October 2001, (b) November 2003, (c) December 2004, (d) October 2005, (e) October 2006, and (f) October 2007.

overcast conditions. Our approach is similar to that of Minnis et al. (1992), but we can take advantage of better in situ validation; the longer dataset and more varied sampling should produce a cloud-top height estimate that can be applied more generally, without regard to location or time of year.

In the next section we put forth our development of a cloud-top height estimate. The corresponding boundary layer lapse-rate estimate is discussed in section 3. Section 4 examines the spatial and diurnal structure of the mean combined October 2005–07 cloud-top height fields constructed for the southeast Pacific at the 4 times of the MODIS overpasses (~1030, 2230, ~0130, and 1330 LT). This is aided by comparison to regional modeling results and coastal observations (primarily Garreaud and Muñoz 2004, 2005; Muñoz and Garreaud 2005; Rutllant et al. 2003). Section 5 discusses the more global implications of the cloud-top height estimate.

2. Development of the cloud-top height estimate

a. Datasets

Individual ship cruise dates, rawindsonde information, and references are given in Table 1. The almost-annual cruises were motivated by the tending of a buoy at 20°S, 85°W, which typically occupied 6–7 days of each cruise. Cooler near-coastal sea surface temperatures (SSTs) reflecting oceanic upwelling are apparent in Fig. 1, with all temperatures, but particularly for those temperatures near the coast showing warming as the Southern Hemisphere moves into its summer (Figs. 1a–c). The October cruises (Figs. 1a,d,e,f) sampled the month of climatologically maximum cloud extent (Klein and Hartmann 1993). Of these, the 2006 and 2007 cruises (Figs. 1e,f) occurred during a warm and cool El Niño–Southern Oscillation (ENSO) phase, respectively.

MODIS cloud-top temperatures (T_{top}), derived from the 11-μm equivalent brightness temperatures, are operationally available from MODIS collection-5 products from both the *Terra* and *Aqua* platforms (King and et al. 2003). The comparison to the radiosondes relies on the level-2 swath data, which have T_{top} values available at 5-km resolution. As determined through the MODIS operational algorithm, the cloudy pixels are first identified and then subsampled (as opposed to averaged) from the original 1-km spatial resolution at nadir to a 5-km spatial resolution. The T_{top} derivation assumes an effective emissivity of one, and corrects for infrared absorption by the overlying water vapor based on National Centers for Environmental Prediction (NCEP) Global Data Assimilation System (GDAS) temperature and humidity values (Menzel et al. 2006).

For the lower boundary, the cloud-top height estimate relies on SSTs derived from the Tropical Rainfall Measurement Mission (TRMM) Microwave Imager (TMI), available as 3-day mean maps at 0.25° resolution (Wentz 1997). The SST retrieval is insensitive to clouds, with little bias compared to buoy data (Gentemann et al. 2004). The TMI SSTs were also independently compared to the ship temperatures derived from a sensor at ~5-cm depth in the ocean. The ship values exceeded the TMI SSTs by 0.3 K in the mean. Infrared cooling of the upper few millimeter of the ocean is estimated to be 0.15–0.20 K (P. Minnett 2008, personal communication), leaving a

TABLE 1. Individual cruise dates, rawindsonde information, and references. Of the 442 total radiosondes, 156 occurred within 1 h of a MODIS overpass under overcast conditions.

Cruise dates	Rawindsonde*	Reference
10–22 Oct 2001	RS-80 (116)	Bretherton et al. (2004)
13–24 Nov 2003	RS-90 (42)	Kollias et al. (2004)
6–22 Dec 2004	RS-92 (71)	Serpetzoglou et al. (2008)
5–20 Oct 2005	RS-90 (70)	N/A
13–27 Oct 2006	RS-93 (71)	N/A
16 Oct–6 Nov 2007	RS-93 (72)	de Szoeke et al. (2009)

* Vaisala type and total number of launches per cruise.

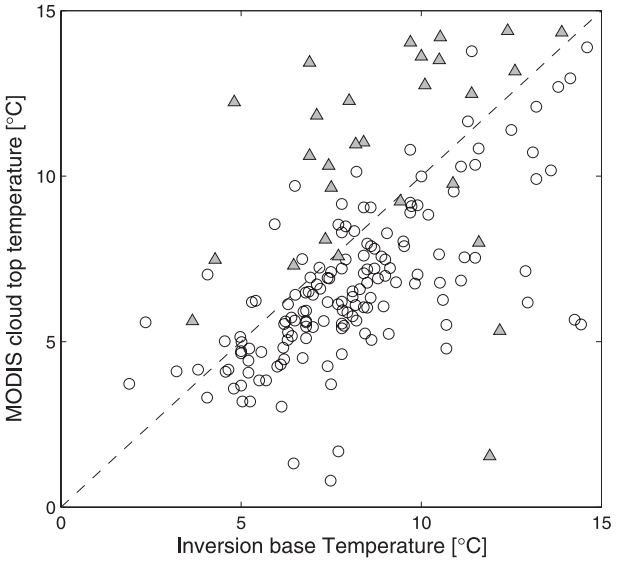

FIG. 2. MODIS T_{top} vs sonde-derived inversion base temperature. The 1-km^2 pixels, classified as cloudy but subsampled from 5-km areas with cloud fractions lower than 0.9 (filled triangles), and overcast pixels (open circles) are indicated.

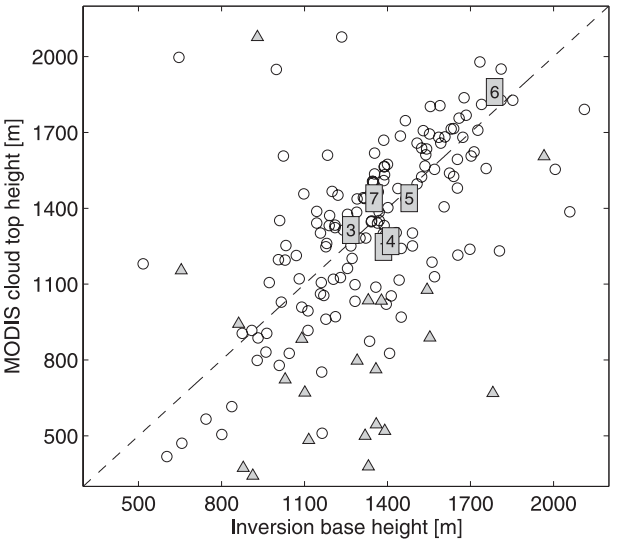

FIG. 3. MODIS cloud-top height, estimated using Eq. (1), vs the sonde-derived inversion base height. Pixels with cloud fractions of 1.0 and <0.9 are indicated as open circles and filled triangles, respectively. Each cruise's 6–7-day mean values at 20°S, 85°W are indicated by the last digit of the cruise's year.

remaining 0.1–0.15-K difference. The TMI's equatorial crossing precesses with time, raising the possibility that a diurnal cycle may become aliased into the TMI 3-day-mean SST. The diurnal cycle in the sea surface temperatures measured from the ship is minimal for this overcast region, however (not shown). In addition, a separate construction of the cloud-top heights using sea surface temperatures measured by the Chilean Navy at San Felix Island (26.5°S, 80°W) did not yield different results.

b. MODIS–radiosonde comparison

In the mean, radar-derived cloud-top heights are most closely associated with the minimum temperature of the cloud-capping inversion base T_{inv}, even though wind profilers indicate that boundary layer tops extend above the inversion base at times, because maximum humidity and temperature gradients occur about 100 m above the inversion base (de Szoeke et al. 2009). MODIS T_{top} values from within 1 h of the satellite overpass are compared to the inversion base temperatures from soundings (T_{inv}) in Fig. 2. Pixels classified as cloudy, but subsampled from 5-km^2 areas with cloud fractions <0.9, typically have a MODIS $T_{top} > T_{inv}$. Surface contamination was a known problem of the previous MODIS collection-4 cloud-top temperature product (e.g., Genkova et al. 2007). Figure 2 suggests that surface contamination remains a problem within collection 5, and perhaps is aggravated if low cloud fractions are preferentially associated with optically thin clouds.

For the overcast (cloud fraction >0.9 over the 5-km^2 area) pixels only, the MODIS-derived cloud-top temperatures are less than the sonde-derived inversion base temperatures by a mean value of 1.3 K, corresponding to a height difference of approximately 150 m. This could be explained by above-cloud NCEP GDAS profiles that are too moist or too warm; however, it may require a different explanation. We leave the investigation of the temperature discrepancy to future work, while accounting for the bias within this study's cloud-top height estimate.

A best-fit line relates the inversion base height z_{inv} (m) to T_{inv} (K) and the 3-day-mean TMI-derived SST (K) according to $\mathrm{SST} - T_{inv} = 0.0069 z_{inv} + 1.05$. We equate z_{inv} to a MODIS cloud-top height z_{top}, and include the 1.3-K offset between T_{top} and T_{inv} in the z_{top} estimate. We find

$$z_{top} = \frac{\mathrm{SST}_{TMI} - T_{top,(MODIS)} - 2.35}{0.0069}, \qquad (1)$$

with SST and T_{top} in kelvins and z_{top} in meters, for cloud tops between 800 and 2000 m. Equation (1) allows an estimate of cloud-top height based on satellite data alone. The comparison between the MODIS z_{top} and the inversion base height (Fig. 3) for the 156 overcast pixels has a correlation coefficient of 0.73, a root-mean-square error of 275 m, and a negligible bias. Values from each cruise follow the same tendency. Cruise-mean values for the 6–7 days spent at the buoy (20°S, 85°W) indicate

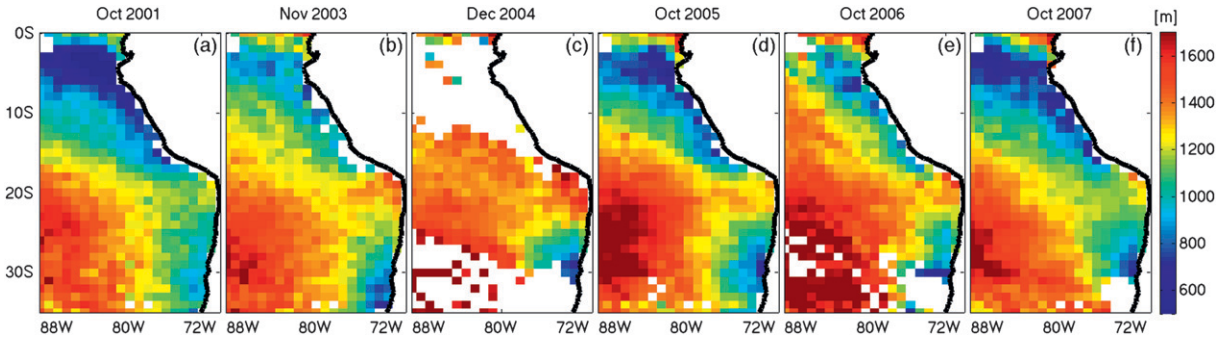

FIG. 4. *Terra* MODIS-derived mean cloud-top heights for each of the cruises, similar to Fig. 1. Separate day and night cloud-top heights were calculated and then averaged together, with monthly mean values only shown if at least one-third of the total possible number of pixels possessed cloud fractions >0.9.

higher cloud-top heights for 2006, which was a warm ENSO year, than for the other years (Fig. 3), but there is no seasonal progression at this distance from the coast. A comparison of z_{top} to the cloud tops defined according to the height of the maximum signal-to-noise ratio within the wind profiler radar returns (de Szoeke et al. 2009) produced more comparison data, but a similar rmse, with the wind profiler placing the mean cloud-top height approximately 50 m higher.

c. Cruise-mean values

Monthly mean cloud-top height maps were developed for each cruise using Eq. (1) (Fig. 4). These were based on the daily level-3 *Terra* MODIS data, which have 1° spatial resolution and report separate day and night values. At 20°S these are basically instantaneous swath values. Monthly mean cloud-top height values were only constructed for those 1° grid cells with cloud fractions (''probably cloudy'' and ''cloudy'' MODIS designations) >0.9, with each reported monthly mean 1° pixel containing at least 10 days worth of data.

In contrast to the buoy-mean values at 20°S, 85°W shown in Fig. 3, cloud-top heights within 10° of the coast rise with the seasonal progression until they dissipate. In the cruise data, a westward tilt is apparent between 75° and 85°W along 20°S in wind profiler–derived boundary layer tops for all of the October cruises (2001, 2005, 2006, and 2007), but not for November 2003 and December 2004. Figures 1 and 4 provide at least a partial climatological explanation, in that the more eastern cloud-top heights lift thermodynamically as the coastal SSTs rise during November and December. October 2006 is also of interest because it is the focus of a modeling assessment. Figure 4 shows that October 2006 cloud tops are the highest of the four October months depicted. October 2006 occurred during a warm ENSO phase, with Fig. 4 indicating decreased boundary layer stability (see also the SSTs in Fig. 1). October 2001 coincided with the Eastern Pacific Investigation of Climate (EPIC) experiment (Bretherton et al. 2004), for which Fig. 4 shows cloud-top heights similar to those of October 2007, despite the warmer SSTs in October 2001 than October 2007. October 2007 occurred during a cool ENSO phase.

3. Boundary layer vertical structure

a. Mean lapse rate

A vertical-mean boundary layer lapse rate can be inferred from Eq. (1) if the sea–air temperature difference is also known. The difference between sea temperatures measured at 5-cm depth and air temperatures measured at 18-m altitude from a flux tower is shown as a function of wind profiler–derived boundary layer height for all the cruises in Fig. 5. Air temperatures were usually less than the sea temperatures, consistent with prevailing cold-air advection. The shallow boundary layers possessed the largest range in sea–air temperature differences, reflecting both cold-air advection such as that associated with the Chilean coastal jet, and warm continental air advected offshore at near-coastal locations (e.g., de Szoeke et al. 2009; Garreaud and Muñoz 2005).

The mean temperature difference of 0.8 K does not vary linearly with cloud-top height. After accounting for a mean 0.3-K SST difference from the ship sensor values, the mean TMI SST–air temperature difference is 0.5 K, similar to that of the NCEP reanalysis (Klein and Hartmann 1993). If a sea–air temperature difference of 0.5 K is assumed, the vertical-mean boundary layer lapse rate $[(T_{air} - T_{inv})/z_{top}; \text{K km}^{-1}]\Gamma_{eff}$ can be estimated through

$$\Gamma_{eff} = 6.9 + 0.55 z_{top}^{-1}, \quad (2)$$

with z_{top} in kilometers and applicable to the range of cloud-top heights falling between 800 and 2000 m. Here,

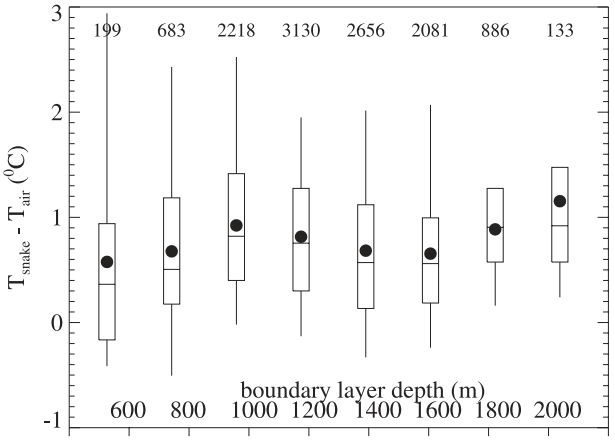

FIG. 5. Difference between 5-cm-depth sea temperature (T_{snake}) and air temperature (T_{air}, 18-m altitude) as a function of boundary layer height, derived from a wind profiler using data from all of the cruises, shown as a box plot with the median value indicated by a line, with the box edges indicating the 25th and 75th percentile values, and with whiskers extending to the 5th and 95th percentile values. Mean values are indicated as filled circles. Boundary layer height is binned by increments of 200 m, with the mean height value indicated below each box plot, and the number of contributing samples given above each box plot.

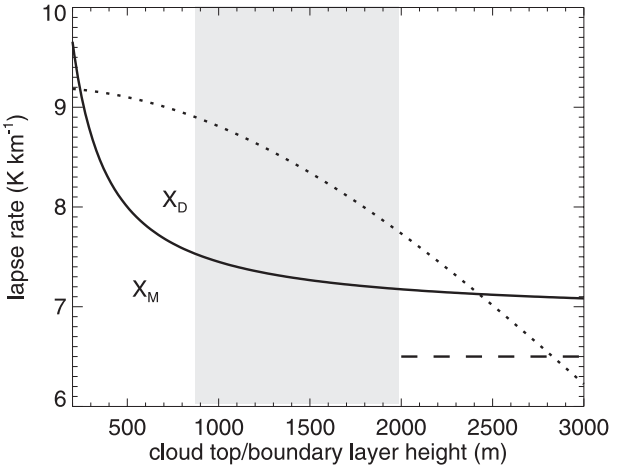

FIG. 6. Boundary layer lapse rate as a function of cloud-top height according to Eq. (2) (solid line) and the Wood and Bretherton (2004) parameterization (dotted line). Respectively, "X_M" and "X_D" indicate the lapse rates inferred by Minnis et al. (1992) and Stevens et al. (2007), and the dashed line corresponds to the climatological lapse-rate value endorsed by Minnis et al. (1992) and Wang et al. (1999). The gray-shaded area shows the range of cloud-top heights sampled within Fig. 3.

Γ_{eff} is what would be inferred from the soundings alone, and it is appealing because it is independent of instrument artifacts, in contrast to Eq. (1). The Γ_{eff} is steepest (7.6 K km^{-1}) for the shallowest boundary layer of 800 m, decreases to 7.2 K km^{-1} for the deepest observed boundary layers of 2 km, and asymptotes to 6.9 K km^{-1} for even deeper layers. As such, the dependence of the lapse rate upon the boundary layer height is weak, with observed values varying by only about 5%.

The boundary layer lapse rate predicted by Eq. (2) for different boundary layer depths is shown in Fig. 6, along with the lapse-rate parameterization of Wood and Bretherton (2004), and other previously reported values. The Wood and Bretherton (2004) lapse rate relies on satellite data only, but accounts for the air–sea temperature difference within the parameterization. Minnis et al. (1992) deduced a mean lapse rate of 7.1 K km^{-1} at inversion heights of ~600 m from aircraft soundings at ~30°N, 120°W. While shallower than the 7.8 K km^{-1} we deduce, the Minnis et al. (1992) value is close to our value for deeper boundary layers and is a reasonable constant lapse-rate choice (e.g., Garreaud et al. 2001). During the Dynamics and Chemistry of Marine Stratocumulus-II experiment, a mean lapse rate of 8 K km^{-1} and mean boundary layer depth of ~760 m was inferred from aircraft data at approximately the same location (Stevens et al. 2007), which is slightly higher than our Γ_{eff}. The climatological value of 6.5 K km^{-1} endorsed by Minnis et al. (1992) and Wang et al. (1999) appears low compared to Γ_{eff}, but we lack data with which to evaluate this. For boundary layer depths <200 m, Γ_{eff} is unphysically high (>9.8 K km^{-1}). A few individual cloud-top heights derived using Eq. (1) for shallow layers are also obviously underestimated in Painemal et al. (2009), while Fig. 3 suggests that a slight underestimation of MODIS cloud-top heights occurs already for inversion bases <900 m. For the range of boundary layer depths sampled by the cruise radiosondes, Γ_{eff} is consistently less than the Wood and Bretherton (2004) lapse rate. One possible explanation may be the surface contamination of the MODIS cloud-top temperature used by Wood and Bretherton (2004). Surface contamination is still apparent in 5-km^2 pixels with cloud fractions <0.9 (Fig. 2), despite a subsampling algorithm intended to discourage this. MODIS collections previous to collection 5 averaged all 1-km^2 pixels to produce a 5-km^2 cloud-top temperature, and the low cloud-top temperature undoubtedly included surface contamination if cloud fraction and cloud optical depth are not thresholded (e.g., Genkova et al. 2007).

b. Implications for cloud structure and entrainment

The inverse dependence of the effective lapse rate Γ_{eff} on the cloud-top height in Eq. (2) accounts empirically for an increased decoupling within the deeper boundary layers and constrains the vertical structure of the boundary layer. If the boundary layer were well mixed, the two contributions to Γ_{eff} would come from dry-adiabatic

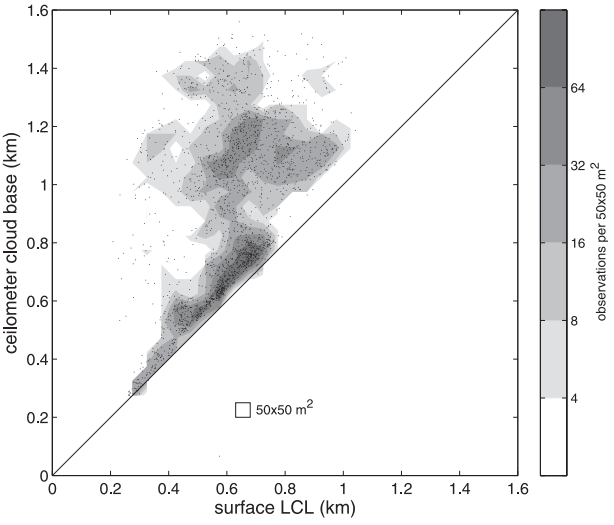

FIG. 7. Ceilometer cloud base vs the 18-m parcel LCL for 10-min data from the 2007 cruise (points). Shaded regions indicate data density per 50 m × 50 m of cloud base–LCL space. The ceilometer data processing reports up to three cloud-base heights per scan, with the highest cloud-base height shown here to reduce drizzle contamination.

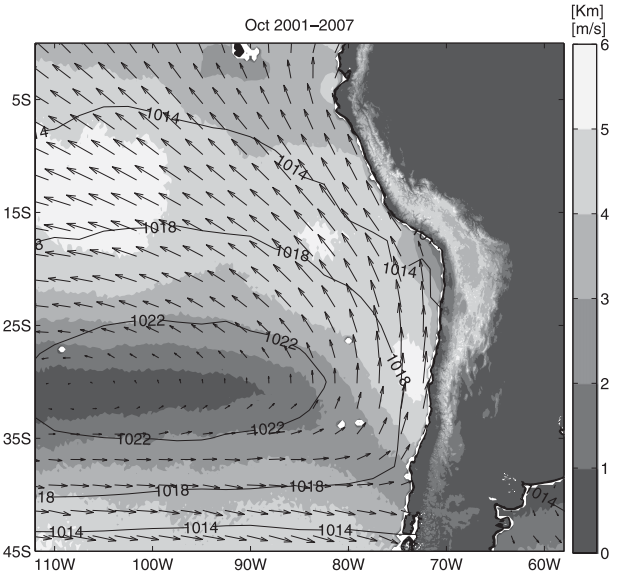

FIG. 8. October-mean (2001–07) NCEP sea level pressure superimposed with corresponding QuikSCAT surface winds and land topography. Shading indicates oceanic wind speeds and land elevations, the latter at 10-min resolution.

mixing within the subcloud layer (a lapse rate of 9.8 K km^{-1}), and moist-adiabatic mixing within the cloud in the presence of water vapor condensation (lapse rate ~6.5 K km^{-1}). Under such conditions the cloud base occurs at the level where water condenses from a lifted and adiabatically cooled surface parcel, or the lifting condensation level (LCL).

We assessed the extent to which the boundary layer was well-mixed by comparing the ceilometer cloud base to the LCL using the 2007 cruise as an example (de Szoeke et al. 2009). Two different cloud bases to LCL relationships were apparent, depending on cloud-base height/boundary layer depth (Fig. 7). Cloud bases between 300 and 800 m corresponded well to the LCL, indicating well-mixed conditions that are consistent with Wood and Bretherton (2004). Even for these clouds, the bases were approximately 10% higher than their corresponding LCL. This could be the result of moisture gradients in the subcloud layer, with the ship sampling moister air at 18 m than was characteristic of most of the subcloud mixed layer (Davidson et al. 1984).

For the higher cloud bases (>800 m), the LCL was most commonly between 600 m and 1 km and the cloud bases were often 200–600-m higher, ranging up to 1.5 km. This should reflect entrainment of dry air into the boundary layer evaporating the base of the stratocumulus cloud, with cumulus plumes within the decoupled layer transporting water vapor from the surface to the stratocumulus layer (Wood and Bretherton 2004; Wyant et al. 1997). In Fig. 7, this decoupled layer is arguably most visible between 800 and 1000 m, corresponding to a gap between the two parts of the distribution where relatively few cloud bases were observed.

4. Regional features

The spatially inhomogeneous cloud-top height fields of Fig. 4 indicate a complex regional climate. We further explored their connection. A guide to the October-mean climatological circulation is provided by Fig. 8, which indicates the NCEP mean sea level pressure, Quick Scatterometer (QuikSCAT) mean surface winds, and land elevation data. The climatological high pressure system is centered at approximately 30°S, 95°W, or ~2000 km off of the South American coast, driving winds anticyclonically with the South American topography, encouraging a coastal jet (Garreaud and Muñoz 2005; Muñoz and Garreaud 2005) that is evident even in the mean wind speeds as a maximum of 6 m s^{-1} at ~30°S. As the surface winds nearly parallel to the coast encounter the Andes of southern Peru, the mean surface wind speeds reduce to <2 m s^{-1} over the Arica Bight at ~20°S, 72°W. Note the height of the Andes is almost 5 km in this region.

The diverse influences on cloud-top height can be expressed through

$$\frac{\partial z_{\text{top}}}{\partial t} = -U\frac{\partial z_{\text{top}}}{\partial x} - V\frac{\partial z_{\text{top}}}{\partial y} + \omega_{\text{en}} - \omega_{\text{MS}} - \omega_{\text{diurnal}}, \qquad (3)$$

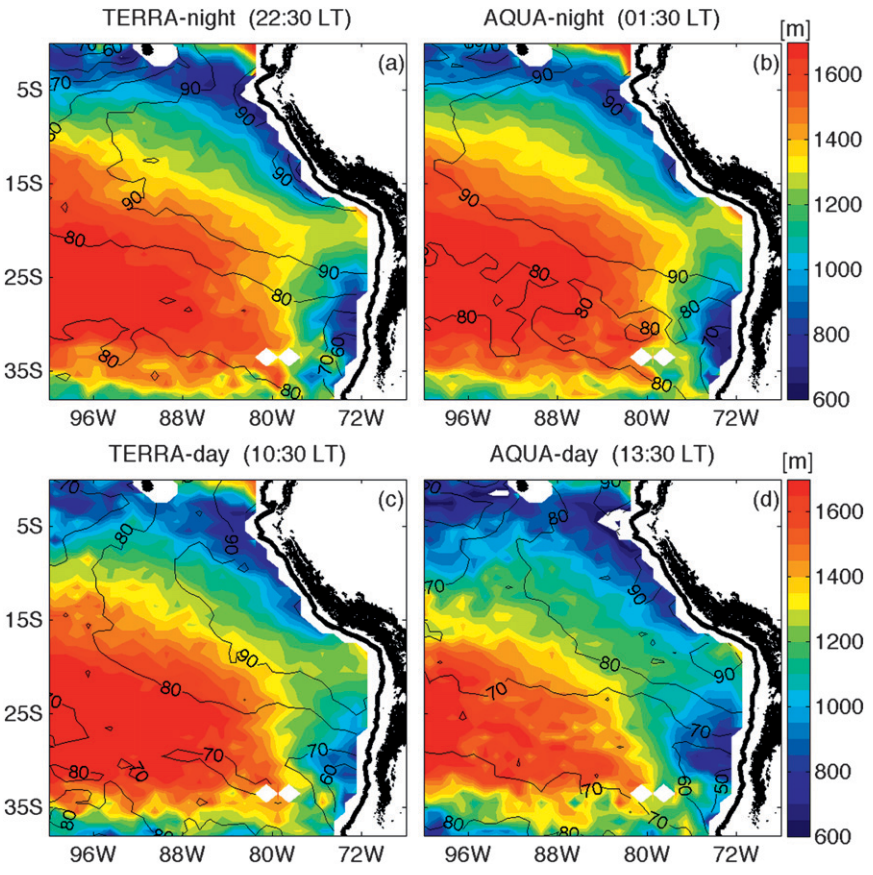

FIG. 9. Mean cloud-top height fields for October 2005, 2006, and 2007 combined for (a) *Terra* night, at 2230 LT, (b) *Aqua* night, at 0130 LT, (c) *Terra* day, at 1030 LT, and (d) *Aqua* day, at 1330 LT. Values are based on the samples possessing a cloud fraction >90% only, with typically at least one-third of all samples contributing when cloud fractions, indicated by the contour lines, exceed 70%. Land elevations exceeding 3 km at 10-min spatial resolution are also indicated.

where the free-tropospheric subsidence at cloud top is decomposed into ω_{MS} and $\omega_{diurnal}$, and ω_{en} is cloud-top entrainment. Here, ω_{MS} includes the large-scale October-mean subsidence associated with the anticyclone, which is evident, for example, in the QuikSCAT surface winds as they quicken and diverge in their easterly equatorward trajectory north of 15°S (Fig. 8). Also, ω_{MS} includes the mesoscale variations in the cloud-top subsidence, including specific, near-coastal features. The $\omega_{diurnal}$ refers to diurnal variations in the free-troposphere subsidence, and includes orographically induced variations felt remotely as an offshore propagation forced by sensible heating of the dry Andes (e.g., Garreaud and Muñoz 2004) or locally through modifications of a land–sea-breeze circulation (e.g., Rutllant et al. 2003).

Three months of MODIS data (October 2005, 2006, and 2007) were combined to reduce sampling noise and to improve elucidation of the regional and diurnal features. The mean cloud-top height fields, with mean cloud fraction values overlaid, are shown at each of the four MODIS overpass times (Fig. 9). In contrast to the International Satellite Cloud Climatology Project (ISCCP), which places the low cloud fraction maximum offshore, west of 90°W [not shown, but see also Fig. 1 in Wood and Hartmann (2006)], the MODIS cloud fraction maximum parallels the coast. One explanation may be that the MODIS cloud mask is better able to discriminate the low near-coastal clouds than ISCCP is. A strong alongshore coastal gradient is apparent in the cloud-top heights, with Peruvian coastal shoaling (a shallowing of the boundary layer evident as lower cloud-top heights) north of 18°S, higher cloud-top heights over the Arica Bight at ~20°S, and lowered cloud-top heights above the Chilean coastal jet between 25° and 35°S. Each region and its diurnal variability are discussed in turn, beginning with the shallower boundary layer regions.

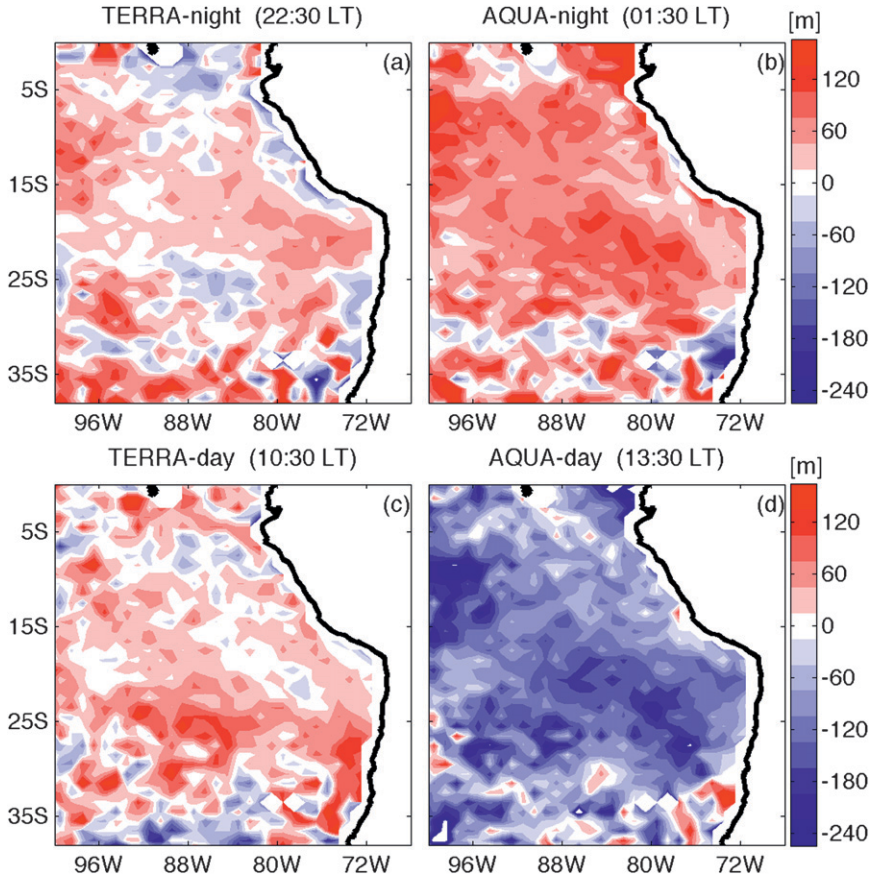

FIG. 10. Same as in Fig. 9, but here cloud-top heights are plotted as the anomaly from the 4-times-daily mean, and cloud fraction is not shown. The panels correspond to (a) *Terra* night, at 2230 LT, (b) *Aqua* night, at 0130 LT, (c) *Terra* day, at 1030 LT, and (d) *Aqua* day, at 1330 LT.

a. Peruvian coastal shoaling

North of 18°S coastal shoaling of the boundary layer is obvious at all times of the day, particularly at 1330 LT (*Aqua* day). Afternoon cloud clearing is frequent (e.g., de Szoeke et al. 2009), which is thought to be encouraged by enhanced afternoon entrainment of warm, dry above-inversion air into the boundary layer (Garreaud and Muñoz 2004), along with shortwave absorption. Are the diurnal changes in cloud-top height consistent with the modeled subsidence diurnal cycle of Garreaud and Muñoz (2004; Fig. 3)? In their results, the coastal boundary layer depth is influenced diurnally by the sensible heating of the dry Andes Mountains affecting the free-tropospheric subsidence, which is apparent as a narrow band of upward motion propagating away from and parallel to the Peruvian coast.

The MODIS cloud-top heights are shown as the anomaly from their 4-times-daily mean in Fig. 10. For *Aqua* day, a suppression of the cloud tops, by almost 250 m in places, is evident 10° to the southwest of the Peruvian coast. The *Terra* night z_{top} anomaly pattern is opposite in phase but of a smaller amplitude, with cloud tops offshore of Peru raised by 25–50 m. The pattern is consistent with Garreaud and Muñoz (2004) while the observed diurnal range of 250–275 m exceeds the modeled ~150-m range. Offshore propagation of a rise in the cloud tops is not as clearly depicted as in the modeled upward velocity values; nevertheless, however, it is suggested in the evolution from the 2230 LT snapshot of *Terra* at night offshore of southern Peru, through 0130 LT *Aqua* at night, to 1030 LT *Terra* at day (Fig. 10a–c), with an approximate speed of 20 m s^{-1}, which is slightly slower (corresponding to a slightly larger vertical wavelength) than those modeled by Garreaud and Muñoz (2004).

b. Chilean coastal jet

Another prominent feature in Fig. 9 is the shallow boundary layer of a coastal jet located approximately between 25° and 35°S (Garreaud and Muñoz 2005; Muñoz and Garreaud 2005), which is also associated

with reduced cloud fractions. The jet's vertical structure has been previously documented, mostly with isolated soundings and in modeling simulations (Garreaud et al. 2001; Garreaud and Muñoz 2005; Muñoz and Garreaud 2005). The jet is located at the inversion capping the boundary layer, with the boundary layer deepening toward the north, which is also evident in Fig. 9. Modeling simulations find enhanced (suppressed) subsidence modeled for the entrance (exit) regions of the Chilean coastal jet (Garreaud and Muñoz 2005; Muñoz and Garreaud 2005). As posited in Muñoz and Garreaud (2005), the root cause of the enhanced stability capping the coastal jet is the orographic channeling, with the frictional deceleration of the almost-meridional winds as they enter the Arica Bight balanced in the equations of motion by easterly zonal winds centered at the height of the inversion, or ~500 m (Garreaud and Muñoz 2005). The warm, dry air advected off of the continent contributes to a stable atmosphere, with the cloud-top heights observed here at ~600 m (Fig. 9).

Figure 9 shows that by the early afternoon the shallow boundary layer associated with the coastal jet is extended both westward and northward. A similar spatial structure is evident in the diurnal amplitude of surface QuikSCAT winds (Fig. 3a; Muñoz 2008; Muñoz and Garreaud 2005). Assuming that the jet winds at the inversion height also have an afternoon maximum, at least some of the increased afternoon offshore shoaling can be explained through the advection term $-V\partial z_{\text{top}}/\partial y$ (primary), and the possibly secondary $-U\partial z_{\text{top}}/\partial x$, consistent with Muñoz (2008), though the root cause must lie with dynamic adjustment to the afternoon coastal sensible heating (e.g., Fig. 9; Garreaud and Muñoz 2004).

c. Arica Bight

The Arica Bight region was well sampled during the VOCALS Regional Experiment (VOCALS-REx) planned for October–November 2008, and is the location of high cloud-droplet number/accumulationmode aerosol concentrations of as-yet undetermined origin(s). Apparent in Fig. 9 is a ridging along 20°S of cloud-top heights, with cloud tops above the Arica Bight ~500 m higher than those to its north or south. The latitudinal strip along 20°S was a common flight path for the VOCALS research aircraft based in Arica, Chile. Though elevated cloud-top heights typify the Arica Bight, they are also higher later in the austral summer and during the warm (2006) ENSO phase (Fig. 4), when the surface waters of the Arica Bight, already slightly warmer than their surroundings, are even warmer still (Fig. 1).

The elevated cloud-top heights above the Arica Bight are enigmatic. They are not obvious in cloud-top height fields derived from the CALIOP instrument (R. Wood and D. Wu 2008, personal communication), which is almost coincident with *Aqua*. Cloud-top height fields derived from the *Terra* day ~400-km-swath Multiangle Imaging Spectraradiometer (MISR) data do show elevated heights above the Arica Bight (M. Garay 2008, personal communication), however, using a completely independent stereographic cloud-top height retrieval. Geoscience Laser Altimeter System measurements also show higher cloud tops above the Arica Bight (Ahlgrimm and Randall 2006).

One explanation is that dynamical blocking by the southern Peruvian Andes of the surface winds at the exit region of the Chilean coastal jet (evident in Fig. 8) encourages convergence and a mean upward motion over the Arica Bight (Muñoz and Garreaud 2005). Figure 9 provides observational confirmation of the deeper boundary layer that would be induced by such mesoscale convergence. In a steady state, Eq. (3) could to first order be reduced to $V\partial z_{\text{top}}/\partial y + U\partial z_{\text{top}}/\partial x = \omega_{\text{MS}}$, with the spatial gradients in the cloud-top height used to estimate a mean upward vertical velocity at the boundary layer top. We estimate a latitudinal change in the cloud-top height of ~600 m/1000 km and assume a mean meridional velocity at the cloud top of 5 m s^{-1} between 20° and 30°S [consistent with Fig. 8 and Garreaud and Muñoz (2005, their Fig. 10)]. If we ignore the longitudinal leaking of convergence, we can estimate an upper bound to ω_{MS} of ~0.3 cm s^{-1} , which is similar to that modeled for the jet exit region (Muñoz and Garreaud 2005, their Fig. 3c), though farther downstream of the jet.

These coastal jet near-surface winds have an afternoon maximum (Garreaud and Muñoz 2005), so that their deceleration into the Arica Bight region should generate an afternoon cloud-top height maximum according to the previous argument. Instead, a minimum is observed in the cloud-top heights in the early afternoon (Figs. 9d and 10d). This suggests that another diurnal physical process must also be active. For this we turn to diurnal variability in the free-tropospheric subsidence, ω_{diurnal}. Coastal radiosonde observations at 23°S have revealed an upper-level land–sea-breeze circulation, driven at the top of the cell by sensible heating of the high-altitude Andes slopes, with divergence from marine stratus cloud-top longwave radiative cooling at the bottom of the circulation cell (Rutllant et al. 2003). The diurnal cycle of this circulation consists of an afternoon subsidence and early morning convergence (Rutllant et al. 2003). Its diurnal variations are broadly consistent with those shown in Fig. 10, although the diurnal range shown in Fig. 10 is more pronounced at 20° than at 23°S, and the nighttime maximum appears to occur earlier slightly farther offshore.

Given that the Andes have elevations of up to 5 km around the Arica Bight (Fig. 8) and the cloud fractions are typically high there (Fig. 9), it seems likely that the Arica Bight boundary layer is influenced by a similar double-cell land–sea-breeze circulation pattern as put forth within Rutllant et al. (2003). The associated subsidence must significantly exceed that induced by the mesoscale dynamical convergence to manifest itself so strongly in the diurnal cloud-top height variability documented here. The mean afternoon zonal subsidence reported by Rutllant et al. (2003) of 1.5 cm s^{-1} supports this. Wood and Bretherton (2004) deduce a mean derived entrainment rate of 0.3–0.4 cm s^{-1} for this region. These values are all consistent with observed cloud-top height drops of ~200 m between *Terra* at night and *Aqua* at day, or ~0.6 cm s^{-1}.

Diurnal sampling may then help explain the MISR and CALIOP cloud-top height fields. According to Fig. 10, the *Terra* day cloud-top heights deviate the least from the 4-times-daily mean, while the *Aqua* day anomalies deviate the most. MISR (*Terra* day) does perceive elevated cloud-top heights over the Arica Bight, while CALIOP (*Aqua* day + night), in addition to being swath limited, does not so much.

5. Implications for other boundary layers

a. October 2008 (VOCALS)

A desire to improve observational knowledge of the larger spatial context for VOCALS-REx of October–November 2008 helped to motivate this work. In this spirit, we show the October 2008 sea surface temperatures and cloud-top heights (Fig. 11). The sea surface temperature field is broadly similar to that of October 2006, but slightly cooler. The mean cloud-top height at 20°S, 85°W is almost 1600 m, which is slightly higher than many of the cruise-mean values, with the exception of October 2006 (Fig. 3). Thus, both October 2006 and October 2008, which are the focus of the modeling assessments, have warmer SSTs and higher cloud-top heights than may be typical.

b. Global distribution

Figure 12 shows the global distribution of boundary layer cloud-top heights for October 2005–07, along with the mean sea surface temperatures, assuming Eq. (1) is valid for all cloud-topped marine boundary layers. We assume for now that above-cloud absorption and scattering of 11-μm radiation in the southeast Atlantic by carbon from biomass burning do not degrade the MODIS T_{top} retrievals (e.g., Bennartz and Harshvardhan 2007).

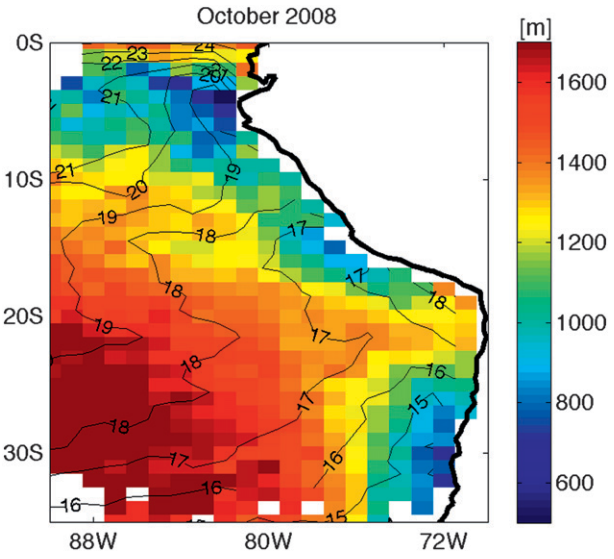

FIG. 11. Cloud-top height fields (color) and TMI sea surface temperatures (contours) for October 2008.

The spatial distribution of low cloud-top heights over the South Pacific follows closely the "dry" zone to the east of the South Pacific convergence zone (Takahashi and Battisti 2007). Here, the cloud-top height spatial structure mirrors the trade winds, with winds both within and above the marine boundary layer acting in concert to advect lower cloud-top heights and cool, dry air equatorward and westward (Richter and Mechoso 2006; Xu et al. 2004). In the southeast Atlantic, the shallow stratocumulus cloud-top heights extend farther to the southwest than for the southeast Pacific. A notable feature is a separate westward extension of depressed cloud-top heights at ~15°S, perhaps influenced by the bulge in the coastline. Model simulations show a Namibian coastal jet approximately similar in size to the Chilean coastal jet (Garreaud and Falvey 2008; Fig. 4a), perhaps most noticeable here as a cloud clearing.

Orography is also thought to influence characteristics of the southeast Atlantic stratocumulus deck, but in a different fashion from the southeast Pacific. As put forth in Richter and Mechoso (2004), in October the boundary layer midlatitude westerlies are deflected equatorward by the Namibian orography, giving rise to the coastal jet feature suggested here and enhancing cold-air advection into the stratocumulus region. Above the boundary layer, however, an anticyclonic circulation centered on the south African continent advects warm, dry continental air southward over the stratocumulus deck (Richter and Mechoso 2004). This differs from the southeast Pacific, and is possible because the coastal mountain range along the Namibian–Angolan coast reaches only ~2-km altitude. While this

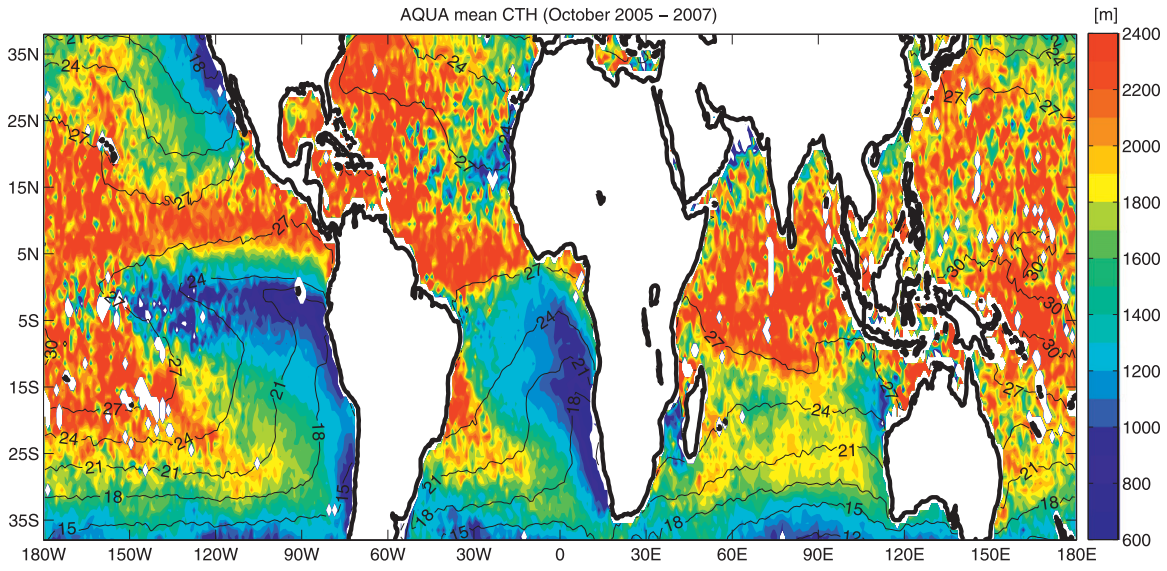

FIG. 12. Mean day + night *Aqua* October 2005, 2006, and 2007 cloud-top heights, with SST indicated as contours. The 40°N–40°S latitude span is set by the TRMM orbit. Only 5-km pixels with warm ($T_{top} > 273$ K) cloud fractions >0.9 are included, with no data threshold set; "noisier" regions indicate less available data.

process is most active in July and August (Richter and Mechoso 2004), the vague definition of the northern boundary to the October low cloud-top height region, in contrast to that in the southeast Pacific, suggests that it also happens here. The lower coastal range may also explain the farther westward extension of the low cloud-top heights for the southeast Atlantic than the southeast Pacific.

6. Conclusions

We empirically derived a height-varying lapse rate from 156 radiosondes, sampling a wide range of southeast Pacific stratocumulus conditions, to develop a cloud-top height estimate relying on the MODIS cloud-top temperature and a satellite microwave-derived sea surface temperature [Eq. (1)]. This circumvents issues with the operational procedures of both MODIS and ISCCP, which tend to place low clouds at too high an altitude (Garay et al. 2008; Harshvardhan et al. 2009; Holz et al. 2008; Wang et al. 1999). Our approach is similar to that of Minnis et al. (1992), but benefits from improved in situ radiosonde validation and exploits a longer dataset. A consistent bias in the MODIS cloud-top temperature (depressed by 1.3 K relative to the sounding inversion base temperature) was accounted for but not explained. Surface contamination of the 5-km^2 MODIS cloud-top temperature was apparent for 5-km^2 cloud fractions <0.9, despite a MODIS collection-5 subsampling algorithm intended to reduce surface contamination compared to the averaging algorithms of previous MODIS collections (Genkova et al. 2007).

Sea–air temperature differences were examined to reconcile a satellite-based estimate of the cloud-top height with lapse rates inferred from soundings. Sea–air temperature differences were most variable for shallow boundary layers, but air temperatures were cooler than the TMI SST by 0.5 K in the mean, consistent with the NCEP reanalysis values for stratocumulus regions (Klein and Hartmann 1993). The sounding-derived lapse rate depends on the cloud-capped marine boundary layer depth, but the dependence is weak, with the lapse rate remaining within 5% of 7.4 K km^{-1} over the range of sampled boundary layer depths. Cloud-base heights measured from the ship coincided with the lifting condensation levels up to cloud bases of ~800 m, indicating well-mixed conditions, consistent with Wood and Bretherton (2004). For the deeper layers, cloud bases were often 200–600 m higher than the lifting condensation level.

The main limitation of the infrared-based technique is its reliance on optically thick cloud cover. An important advantage to using MODIS data, however, is its larger spatial coverage compared to other new satellite platforms (CloudSat and CALIOP, in particular), while the high radiometric calibration allows MODIS to discriminate low-lying near-coastal stratocumulus that may be missed by ISCCP. We focused primarily on spatially coarser (1° resolution) regional characterization within this study, but the swath-level data have also been used to elucidate day-to-day synoptic cloud-top height

variations at San Felix Island (26.5°S, 80°W; see Painemal et al. 2009), and can be similarly applied to characterize VOCALS-REx. The ability to resolve synoptic variability is particularly valuable as the impact of synoptics upon stratocumulus decks becomes appreciated more fully. One strength of this study's empiricism is that the cloud-top height estimate can be used as a model diagnostic.

The larger-scale satellite view was used to characterize regional and diurnal cloud-top height variations, primarily of the southeast Pacific stratocumulus deck. These document features seen previously in model simulations and more limited observations. The more noteworthy findings for the southeast Pacific include the following:

- There is a diurnal range in cloud-top heights of up to 250 m, which is larger than that in the model simulations of Garreaud and Muñoz (2004). This may be because the observed cloud-top heights are higher than the modeled values, and they experience larger variations in the free-tropospheric subsidence.
- There are elevated cloud-top heights above the Arica Bight that are consistent with a modeled mesoscale mean upward motion (Garreaud and Muñoz 2005; Muñoz and Garreaud 2005), but are not yet observationally documented.
- There is an afternoon expansion of the boundary layer height to the north and west of the Chilean coastal jet that is spatially similar to the evening–morning difference in QuikSCAT surface winds (Muñoz 2008).
- There is a strong diurnal cycle in the cloud-top heights above the Arica Bight, with a significant depression of the afternoon cloud-top heights. Surface contamination of the afternoon retrievals may contribute, but the diurnal change is also consistent with competing influences from an afternoon increase in mesoscale convergence at the Chilean coastal jet exit region (e.g., Muñoz 2008) and increased afternoon subsidence (Rutllant et al. 2003).
- There is a seasonal progression, with warmer waters and higher cloud tops near the coast, as the Southern Hemisphere moves into its summer. This acts to reduce a longitudinal gradient in boundary layer height along 20°S, which is evident in the October months. The two October months intended for modeling assessments (2006 and 2008) both have slightly warmer SSTs and slightly higher cloud-top heights than the other October months examined (2001, 2005, and 2007).

Findings for the southeast Atlantic include the following:

- There is a larger westward spatial extent and a more vaguely defined northern boundary than is true of the southeast Pacific deck. This is consistent with the lower Namibian/Angolan coastal range (~2-km elevation) relative to the Andes, allowing for more offshore transport of warm, dry air capping the stratocumulus temperature inversion.
- There is a separate, unexplained westward extension of the southeast Atlantic stratocumulus deck at 15°S, accompanied by a slightly more depressed near-coastal cloud-topped boundary layer at this latitude. Otherwise, coastal shoaling is less latitudinally varying than for the southeast Pacific.

Some differences from other satellite measures of cloud-top height can be explained through spatial or temporal sampling differences. The 1030 LT (*Terra* day) MODIS overpass is the most similar to the diurnal mean of the four irregularly timed overpasses. CALIOP is assumed to measure cloud-top heights accurately, including the thin broken clouds that are problematic for infrared-based techniques, but CALIOP did not capture the elevated cloud tops above the Arica Bight within a 1-month mean sample, hampered by its limited swath and *Aqua* temporal sampling. Cloud-top heights derived from the MISR, despite a swath width of only one-sixth that of MODIS, characterized the Arica Bight elevated cloud-top heights reasonably well because the sampling occurs at 1030 LT (*Terra* day).

We still need to establish more careful error bars for the estimate [Eq. (1)] developed here. A root-mean-square error of 275 m exists between the MODIS z_{top} and radiosonde temperature inversion height in Fig. 3, but this value will be dominated by field-of-view differences. Another error estimate comes from the difference of 50 m between the ship-based wind profiler cloud-top heights and radiosonde temperature inversion. A more thorough comparison to cloud-top heights derived from CALIOP is planned. Another issue we wish to address is the high values of ISCCP midlevel cloud reported over the southeast Pacific stratocumulus region (e.g., Fig. 1; Wood and Hartmann 2006); these cloud fractions exceed our expectations for the ISCCP operational misidentification of low cloud-top height. The work presented here was undertaken as part of a larger ongoing study examining synoptic variability on aerosol–cloud–precipitation interactions, to which these empirically derived cloud-top heights will contribute.

Acknowledgments. Support from the NOAA Climate Program for the Prediction of the Americas (CPPA Grant NA06OAR4310056) for PZ and DP, and CPPA Grants GC07-095 and GC06-087 for SdS and CF, is gratefully acknowledged. The TMI data were produced by Remote Sensing Systems and sponsored by the NASA Earth Science REASoN DISCOVER Project, and are available online (http://www.remss.com), along

with QuikSCAT winds. The MODIS data were acquired from the Goddard Distributed Active Archive Center (DAAC). Land elevation data at 10-min resolution are from the U.S. Navy Fleet Numerical Oceanography Center and are also available online (http://www.dss.ucar.edu/datasets). We thank René Garreaud for illuminating discussion, Michael Garay and Rob Wood for comments and plots of October 2006 MISR and CALIOP cloud-top height, Rob Burgman and Amy Clement for discussion and inspiration, and Shang-Ping Xie for originally suggesting to us the desirability of characterized boundary layer cloud-top heights. Two anonymous reviewers contributed, and we wish to thank one in particular for valuable comments.

REFERENCES

Ahlgrimm, M., and D. Randall, 2006: Diagnosing monthly mean boundary layer properties from reanalysis data using a bulk boundary layer model. *J. Atmos. Sci.,* **63,** 998–1012.

Bennartz, R., and Harshvardhan, 2007: Correction to ''Global assessment of marine boundary layer cloud droplet number concentration from satellite.'' *J. Geophys. Res.,* **112,** D16302, doi:10.1029/2007JD008841.

Betts, A. K., P. Minnis, W. Ridgway, and D. F. Young, 1992: Integration of satellite and surface data using a radiative-convective oceanic boundary-layer model. *J. Appl. Meteor.,* **31,** 340–350.

Brest, C. L., W. B. Rossow, and M. D. Roiter, 1997: Update of radiance calibrations for ISCCP. *J. Atmos. Oceanic Technol.,* **14,** 1091–1109.

Bretherton, C. S., and Coauthors, 2004: The EPIC 2001 stratocumulus study. *Bull. Amer. Meteor. Soc.,* **85,** 967–977.

Davidson, K. L., C. W. Fairall, P. Jones-Boyle, and G. E. Schacher, 1984: Verification of an atmospheric mixed-layer model for a coastal region. *J. Climate Appl. Meteor.,* **23,** 617–683.

de Szoeke, S., C. W. Fairall, and S. Pezoa, 2009: Ship observations coasting South America in the tropical Pacific Ocean. *J. Climate,* **22,** 458–464.

Garay, M. J., S. P. de Szoeke, and C. M. Moroney, 2008: Comparison of marine stratocumulus cloud top heights in the southeastern Pacific retrieved from satellites with coincident ship-based observations. *J. Geophys. Res.,* **113,** D18204, doi:10.1029/2008JD009975.

Garreaud, R. D., and R. Muñoz, 2004: The diurnal cycle of circulation and cloudiness over the subtropical southeast Pacific: A modeling study. *J. Climate,* **17,** 1699–1710.

——, and ——, 2005: The low-level jet off the west coast of subtropical South America: Structure and variability. *Mon. Wea. Rev.,* **133,** 2246–2261.

——, and M. Falvey, 2008: The coastal winds off western subtropical South America in future climate scenarios. *Int. J. Climatol.,* **29,** 543–554, doi:10.1002/joc.1716.

——, J. Rutllant, J. Quintana, J. Carrasco, and P. Minnis, 2001: CIMAR-5: A snapshot of the lower troposphere over the subtropical southeast Pacific. *Bull. Amer. Meteor. Soc.,* **82,** 2193–2207.

Genkova, I., G. Seiz, P. Zuidema, G. Zhao, and L. D. Girolamo, 2007: Cloud top height comparisons from ASTER, MISR, and MODIS for trade wind cumuli. *Remote Sens. Environ.,* **107,** 211–222.

Gentemann, C. L., F. J. Wentz, C. A. Mears, and D. K. Smith, 2004: In situ validation of Tropical Rainfall Measuring Mission microwave sea surface temperatures. *J. Geophys. Res.,* **109,** C04021, doi:10.1029/2003JC002092.

Hannay, C., D. Williamson, J. Hack, J. Kiehl, J. Olson, S. Klein, C. Bretherton, and M. Kohler, 2009: Evaluation of forecasted simulated southeast Pacific stratocumulus in the NCAR, GFDL, and ECMWF models. *J. Climate,* **22,** 2871–2889.

Harshvardhan, G. Zhao, L. Di Girolamo, and R. N. Green, 2009: Satellite-observed location of stratocumulus cloud-top heights in the presence of strong inversions. *IEEE Trans. Geosci. Remote Sens.,* **47,** 1421–1428, doi:10.1109/TGRS.2008.2005406.

Holz, R. E., S. A. Ackerman, F. W. Nagle, R. Frey, S. Dutcher, R. E. Kuehn, M. A. Vaughan, and B. Baum, 2008: Global Moderate Resolution Imaging Spectroradiometer (MODIS) cloud detection and height evaluation using CALIOP. *J. Geophys. Res.,* **113,** D00A19, doi:10.1029/2008JD009837.

King, M. D., and Coauthors, 2003: Cloud and aerosol properties, precipitable water, and profiles of temperature and water vapor from MODIS. *IEEE Trans. Geosci. Remote Sens.,* **41,** 442–458.

Klein, S. A., and D. L. Hartmann, 1993: The seasonal cycle of low stratiform clouds. *J. Climate,* **6,** 1587–1606.

Kollias, P., C. W. Fairall, P. Zuidema, J. Tomlinson, and G. A. Wick, 2004: Observations of marine stratocumulus in the SE Pacific during the PACS 2003 cruise. *Geophys. Res. Lett.,* **31,** L22110, doi:10.1029/2004GL020751.

Leon, D. C., Z. Wang, and D. Liu, 2008: Climatology of drizzle in marine boundary layer clouds based on 1 year of data from CloudSat and Cloud-Aerosol Lidar and Infrared Pathfinder Satellite Observations (CALIPSO). *J. Geophys. Res.,* **113,** D00A14, doi:10.1029/2008JD009835.

Menzel, W. P., R. A. Frey, B. A. Baum, and H. Zhang, 2006: Cloud top properties and cloud phase algorithm theoretical basis document. MODIS Doc. MOD06CT/MYD06CT-ATBD-C005, 56 pp. [Available online at http://modis-atmos.gsfc.nasa.gov/_docs/MOD06CT:MYD06CT_ATBD_C005.pdf.]

Minnis, P., P. Heck, D. Young, C. Fairall, and J. B. Snider, 1992: Stratocumulus cloud properties from simultaneous satellite and island-based instrumentation during FIRE. *J. Appl. Meteor.,* **31,** 317–339.

Muñoz, R. C., 2008: Diurnal cycle of surface winds over the subtropical southeast Pacific. *J. Geophys. Res.,* **113,** D13107, doi:10.1029/2008JD009957.

——, and R. D. Garreaud, 2005: Dynamics of the low-level jet off the west coast of subtropical South America. *Mon. Wea. Rev.,* **133,** 3661–3677.

O'Dell, C. W., F. J. Wentz, and R. Bennartz, 2008: Cloud liquid water path from satellite-based passive microwave observations: A new climatology over the global oceans. *J. Climate,* **21,** 1721–1739.

Richter, I., and C. R. Mechoso, 2004: Orographic influences on the annual cycle of Namibian stratocumulus clouds. *Geophys. Res. Lett.,* **31,** L24108, doi:10.1029/2004GL020814.

——, and ——, 2006: Orographic influences on subtropical stratocumulus. *J. Atmos. Sci.,* **63,** 2585–2601.

Rozendaal, M. A., C. B. Leovy, and S. A. Klein, 1995: An observational study of diurnal variations of the marine stratiform clouds. *J. Climate,* **8,** 1795–1809.

Rutllant, J. A., H. Fuenzalida, and P. Aceituno, 2003: Climate dynamics along the arid northern coast of Chile: The 1997–1998 Dinamica del Clima de la Región de Antofagasta (DICLIMA) experiment. *J. Geophys. Res.,* **108,** 4538, doi:10.1029/2002JD003357.

Serpetzoglou, E., B. Albrecht, P. Kollias, and C. W. Fairall, 2008: Boundary layer, cloud, and drizzle variability in the southeast Pacific stratocumulus regime. *J. Climate,* **21,** 6191–6214.

Stevens, B., S. Bordoni, C. Holloway, V. Savic-Jovcic, Y. Zhang, A. Beljaars, M. Kohler, and S. Krueger, 2007: On the structure of the lower troposphere in the summertime stratocumulus regime of the northeast Pacific. *Mon. Wea. Rev.,* **135,** 985–1005.

Takahashi, K., and D. S. Battisti, 2007: Processes controlling the mean tropical Pacific precipitation pattern. Part II: The SPCZ and the southeast Pacific dry zone. *J. Climate,* **20,** 5696–5706.

Várnai, T., and A. Marshak, 2002: Observations of three-dimensional radiative effects that influence MODIS cloud optical thickness retrievals. *J. Atmos. Sci.,* **59,** 1607–1618.

von Engeln, A., J. Teixeira, J. Wickert, and S. A. Buehler, 2005: Using CHAMP radio occultation data to determine the top altitude of the planetary boundary layer. *Geophys. Res. Lett.,* **32,** L06815, doi:10.1029/2004GL022168.

Wang, J., W. B. Rossow, T. Uttal, and M. Rozendaal, 1999: Variability of cloud vertical structure during ASTEX observed from a combination of rawinsonde, radar, ceilometer, and satellite. *Mon. Wea. Rev.,* **127,** 2484–2502.

Wang, Y., S.-P. Xie, H. Xu, and B. Wang, 2004: Regional model simulations of marine boundary layer clouds over the southeast Pacific off South America. Part I: Control experiment. *Mon. Wea. Rev.,* **132,** 274–296.

Wentz, F. J., 1997: A well-calibrated ocean algorithm for SSM/I. *J. Geophys. Res.,* **102,** 8703–8718.

Wood, R., and C. S. Bretherton, 2004: Boundary layer depth, entrainment, and decoupling in the cloud-capped subtropical and tropical marine boundary layer. *J. Climate,* **17,** 3576–3588.

——, and D. L. Hartmann, 2006: Spatial variability of liquid water path in marine boundary layer clouds: The importance of mesoscale cellular convection. *J. Climate,* **19,** 1748–1764.

Wyant, M. C., C. S. Bretherton, H. A. Rand, and D. E. Stevens, 1997: Numerical simulations and a conceptual model for the stratocumulus to trade cumulus transition. *J. Atmos. Sci.,* **54,** 168–182.

——, and Coauthors, 2007: A single-column model intercomparison of a heavily drizzling stratocumulus-topped boundary layer. *J. Geophys. Res.,* **112,** D24204, doi:10.1029/2007JD008536.

Xu, H., Y. Wang, and S.-P. Xie, 2004: Effects of the Andes on eastern Pacific climate: A regional atmospheric model study. *J. Climate,* **17,** 589–602.

Zuidema, P., and B. Mapes, 2008: Cloud vertical structure observed from space and ship over the Bay of Bengal and eastern tropical Pacific. *J. Meteor. Soc. Japan,* **86A,** 205–218.